Supplementary Information

Hierarchical RuO_2/Co_3O_4 Heterostructures Enable Efficient Bromine-Mediated Electrochemical Ethylene Epoxidation via Electronic and Structural Synergy

Lvming Zhu[a,b], Zeshuo Meng[a,b], Guang Yang[a,b], Chunyu Zhang[a,b], Xunhua Zhao[c], Yu Kang[a,b], Yi Cui[a,b]**

[a]*School of Nano Technology and Nano Bionics, University of Science and Technology of China, Hefei, 230026, China.*

[b]*i-lab, Vacuum Interconnected NanoTech Workstation (Nano-X), Suzhou Institute of Nano-Tech and Nano-Bionics, Chinese Academy of Sciences, Suzhou 215123, China.*

[c]*School of Physics, Southeast University, Nanjing, 211189, China.*

1. Materials and Reagents

Ruthenium(III) chloride trihydrate ($RuCl_3 \cdot 3H_2O$, [37% Ru, TCI]), Cobalt(II) nitrate hexahydrate ($Co(NO_3)_2 \cdot 6H_2O$, [99%, Aladdin]), Urea ($CO(NH_2)_2$, [99%, TCI]), and Ethanol (C_2H_5OH, [99.5%, Aladdin]). Carbon paper (YLS-30T) was obtained from Sinero®. Potassium bromide (KBr, [AR, Sinopharm]), Sodium perchlorate ($NaClO_4$, [AR, Sinopharm]), Dimethyl sulfoxide (DMSO, [99.7%, Adamas-beta®]), and Ethylene oxide (EO) standard solution (10 mg/mL, [99.9%, TENGZHOU ZHONGKE SPECTRAL ANALYSIS INSTRUMENT CO.,LTD]). All chemicals were used as received without further purification. Deionized water (18.2 MΩ·cm) was used throughout the experiments. All chemicals were used as received without further purification.

2. Synthesis of RuO_2/Co_3O_4 Heterostructures

In a typical synthesis, 1.5 mmol of $Co(NO_3)_2 \cdot 6H_2O$, 0.15 mmol of $RuCl_3 \cdot 3H_2O$, and 6 mmol of urea were dissolved in a mixed solvent containing 40 mL of deionized water and 40 mL of ethanol. The solution was stirred magnetically for 10 minutes to ensure homogeneity. Subsequently, the mixture was transferred into a 100 mL Teflon-lined stainless steel autoclave. A piece of cleaned carbon paper (YLS-30T) was immersed in the reaction solution as the substrate. The autoclave was sealed and maintained at 100 °C for 10 hours. After the hydrothermal reaction, the autoclave was allowed to cool to room temperature naturally. The resulting precursor was collected, washed thoroughly with deionized water and ethanol, and then dried in a vacuum oven at 60 °C overnight. Finally, the dried precursor was annealed in air at 350 °C for 2.5 hours with a heating ramp rate of 5 °C min^{-1} to obtain the RuO_2/Co_3O_4 nanorod arrays.

3. Material Characterizations

The crystal structure and phase composition of the as-prepared samples were analyzed by X-ray diffraction (XRD) using a Bruker AXS D8 Advance X-ray diffractometer with a Cu Kα radiation target (40 V, 40 A) in the 2θ range of 10°–80°. The morphology of the catalysts was examined by field-emission scanning electron microscopy (FESEM, Regulus 8230, Hitachi). The microstructure, lattice fringes, and elemental distribution were further characterized by transmission electron microscopy (TEM) using an FEI Tecnai G2F20 microscope equipped with an energy-dispersive X-ray spectroscopy (EDS) system.

The surface chemical states and elemental composition were determined by X-ray photoelectron spectroscopy (XPS) using an ESCALAB 250Xi XPS instrument with Al Kα X-rays as the excitation source, operated at 15 kV and 10 mA. All binding energies were calibrated using the

adventitious C 1s peak at 284.8 eV as the reference. Raman spectra were recorded on a Renishaw inVia Qontor confocal Raman microscope with a 532 nm laser excitation source. For in situ Raman measurements, the electrochemical cell was placed under the microscope objective, and spectra were collected potentiostatically at various applied potentials to monitor the structural evolution of the electrode surface during the reaction.

4. Electrochemical Measurements

The electrochemical performance was evaluated on a CHI760E electrochemical workstation (Shanghai Chenhua Co., China) using a standard three-electrode system. A carbon rod and an Ag/AgCl electrode (saturated KCl) were used as the counter and reference electrodes, respectively. The working electrode was prepared using a slurry coating method. Typically, 5 mg of the as-synthesized RuO_2/Co_3O_4 catalyst powder was dispersed in a mixture of 250 μL deionized water, 250 μL isopropanol, and 20 μL of Nafion 117 solution. The mixture was sonicated for at least 30 minutes to form a homogeneous catalyst ink. Subsequently, a specific volume of the ink was drop-casted onto a piece of carbon paper (YLS-30T) and dried at room temperature to serve as the working electrode.

The bromine evolution reaction (BrER) tests were primarily conducted in a 0.5 M KBr aqueous electrolyte. Linear sweep voltammetry (LSV) curves were collected at a scan rate of 5 mV s^{-1} to evaluate the catalytic activity. All potentials reported were recorded against the Ag/AgCl reference electrode and were not corrected for iR compensation. Tafel slopes were derived from the LSV curves by plotting the overpotential against the logarithm of current density (log|j|). The electrochemical impedance spectroscopy (EIS) measurements were carried out in the frequency range from 100 kHz to 0.01 Hz with an AC amplitude of 5 mV at the open circuit potential. The electrochemical active surface areas (ECSAs) were estimated from the electrochemical double-layer capacitance (C_{dl}), which was determined by cyclic voltammetry (CV) in the non-Faradaic potential region of 0.6 to 0.7 V vs. Ag/AgCl at various scan rates. The long-term durability was evaluated using chronopotentiometry at a constant current density of 50 mA cm^{-2}.

5. DFT Computational Method

All the density functional theory (DFT) calculations were performed using the Vienna Ab-initio Simulation Package (VASP)[1-4]. The projector augmented wave (PAW) method was employed to describe the ion-electron interactions, and the generalized gradient approximation (GGA) with the Perdew-Burke-Ernzerhof (PBE) functional was used to describe the electron-electron exchange

correlation[3, 5]. To accurately account for the van der Waals interactions, Grimme's DFT-D3 dispersion correction method was adopted[6, 7]. The kinetic energy cutoff for the plane-wave expansion was set to 520 eV.

The atomic model of the RuO_2/Co_3O_4 heterojunction was constructed by interfacing the Co_3O_4 surface with the RuO_2 species. A vacuum space of 15 Å was introduced to avoid interactions between periodic images. For the geometry optimization, the Brillouin zone was sampled using a Gamma-centered k-point mesh of 2 × 1 × 1. The structural relaxation was continued until the forces on all atoms converged to less than 0.05 eV $Å^{-1}$[8, 9], and the energy convergence criterion was set to 10^{-4} eV. Electronic smearing was treated using the Gaussian method with a width of 0.05 eV. Spin polarization was included in all calculations to account for the magnetic properties of the cobalt and ruthenium species.

The Gibbs free energy change (ΔG) for the reaction steps was calculated based on the computational hydrogen electrode (CHE) model proposed by Nørskov et al., using the equation: $\Delta G = \Delta E + \Delta ZPE - T\Delta S$, where ΔE is the reaction energy difference obtained from DFT calculations. The thermodynamic correction terms (ΔZPE and TΔS) were calculated using the VASPKIT code based on the vibrational frequencies.[9, 10]

DFT calculations were performed using a vacuum slab model combined with the computational hydrogen electrode (CHE) model. To directly evaluate the intrinsic electronic interactions at the RuO_2/Co_3O_4 interface, explicit solvent and electric field effects were deliberately excluded. This simplified model accurately predicts the relative trends in catalytic activity, yielding results highly consistent with our experimental observations. Introducing complex solvation models would significantly increase computational costs without altering the core conclusions regarding this interfacial synergistic effect.

6. Calculation of Faradaic Efficiency

The Faradaic efficiency (FE) for the electrosynthesis of ethylene oxide (EO) was calculated by comparing the experimentally determined moles of EO (n_{exp}) with the theoretical moles (n_{theo}) assuming 100% current efficiency.

First, the total charge (Q, in Coulombs) passed through the electrolytic cell was calculated using the equation $Q = I \times t$, where I is the applied current (in Amperes) and t is the electrolysis time (in seconds). For a typical stability test conducted at 50 mA for 1 hour, the total charge passed is 180 C ($0.05\ A \times 3600\ s$).

Second, the theoretical molar yield of EO (n_{theo}) was calculated based on Faraday's law. Since the formation of one EO molecule involves a two-electron transfer process $(n = 2)$, the theoretical yield is expressed as:

$$n_{theo} = \frac{Q}{n \times F} = \frac{I \times t}{2 \times F}$$

where F is the Faraday constant $96485\ C\ mol^{-1}$).

Finally, the actual moles of EO product (n_{exp}) were quantified by ^{1}H NMR spectroscopy using DMSO as the internal standard. The Faradaic efficiency was then determined by the ratio of the actual yield to the theoretical yield:

$$FE = \frac{n_{exp}}{n_{theo}} \times 100\%$$

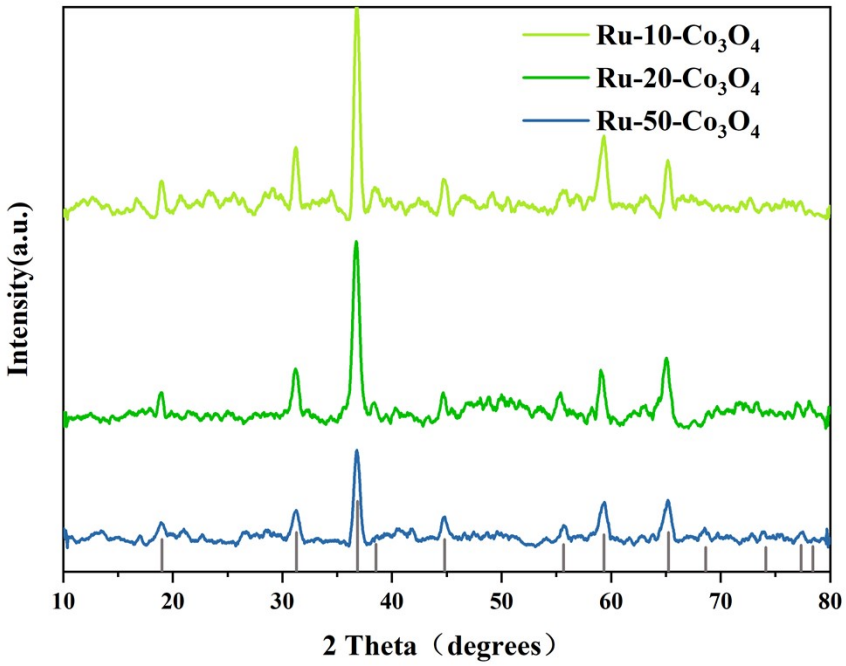

Figure S1. XRD patterns of Ru-Co_3O_4 composites with different Ru loadings (Ru-10, Ru-20, and Ru-50). The diffraction peaks corresponding to the spinel Co_3O_4 phase are clearly visible. With increasing Ru loading, the diffraction features associated with Ru species evolve, confirming the successful incorporation of Ru into the composite.

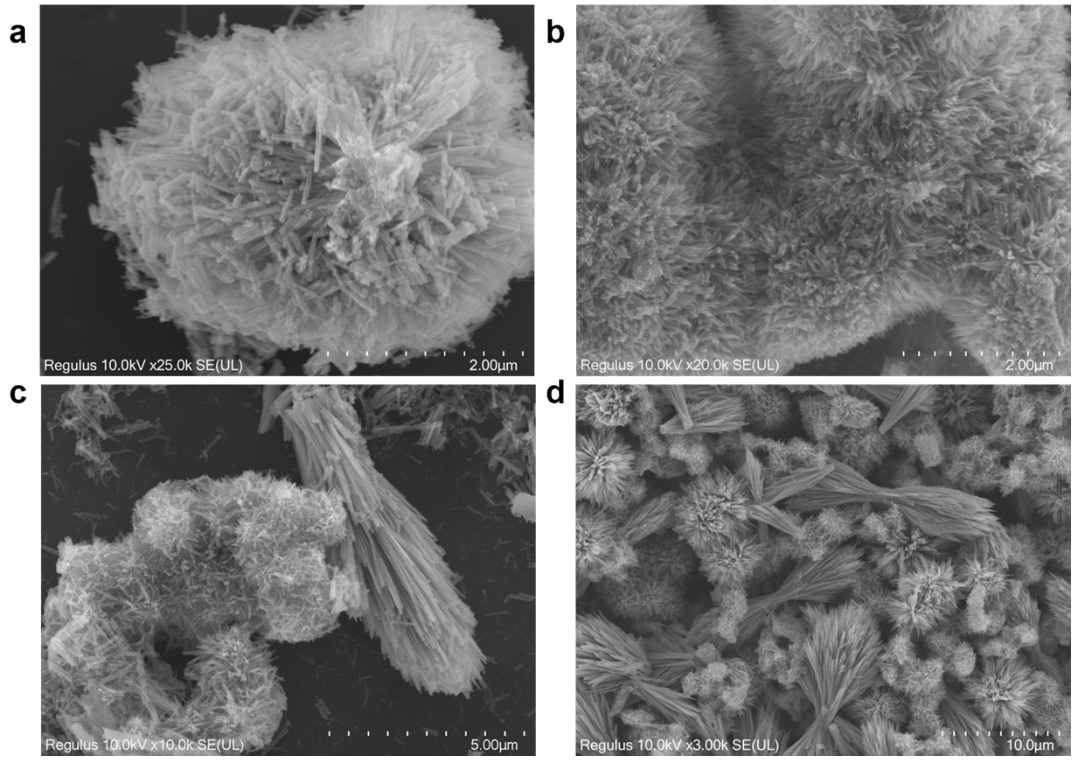

Figure S2. (a-d) Additional SEM images of the RuO_2/Co_3O_4 catalyst at different magnifications. The images reveal the dense, hierarchical "flower-like" or "urchin-like" cluster morphology composed of numerous radially oriented nanorods. This open framework structure facilitates electrolyte penetration and gas diffusion.

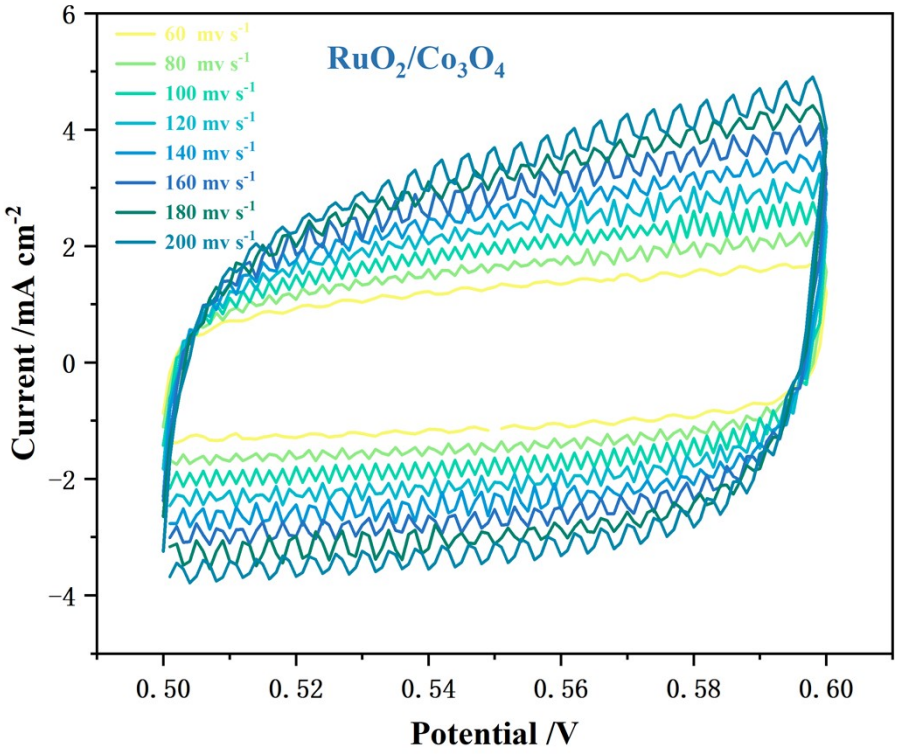

Figure S3. Cyclic voltammetry (CV) curves of RuO_2/Co_3O_4 catalyst measured in a non-Faradaic potential window (0.60–0.70 V vs. Ag/AgCl) at scan rates of 60, 80, 100, 120, 140, 160, 180, and 200 mV s^{-1}.

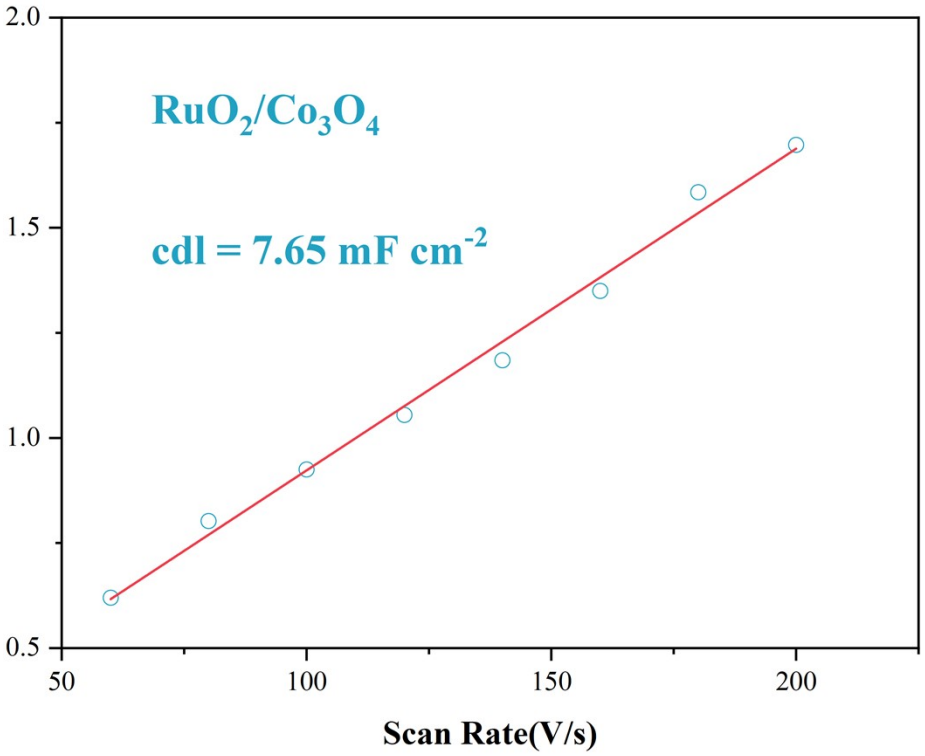

Figure S4. Linear fitting of the capacitive current density differences ($Delta\, j = (j_a - j_c)/2$ at 0.65 V) versus scan rates for RuO_2/Co_3O_4.

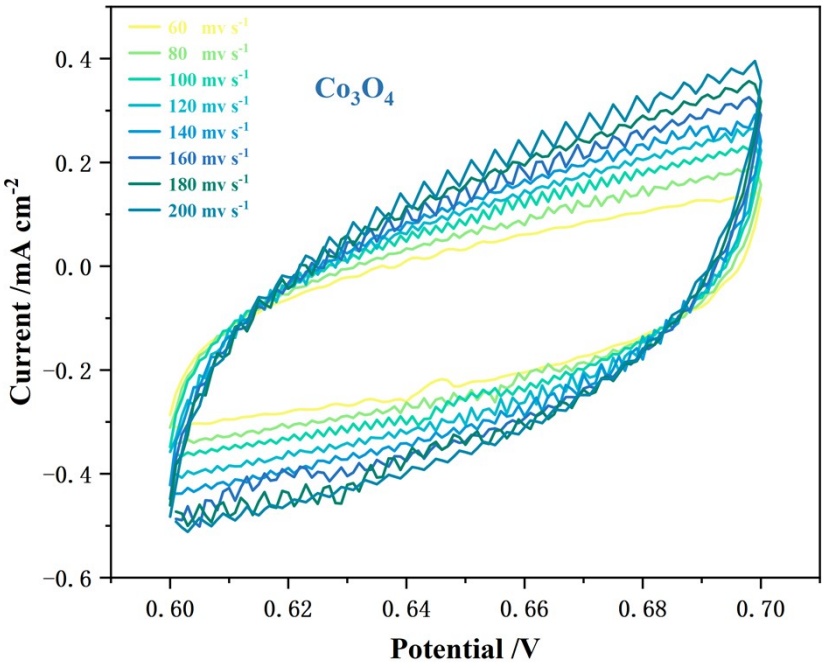

Figure S5. CV curves of pure Co_3O_4 catalyst under the same conditions.

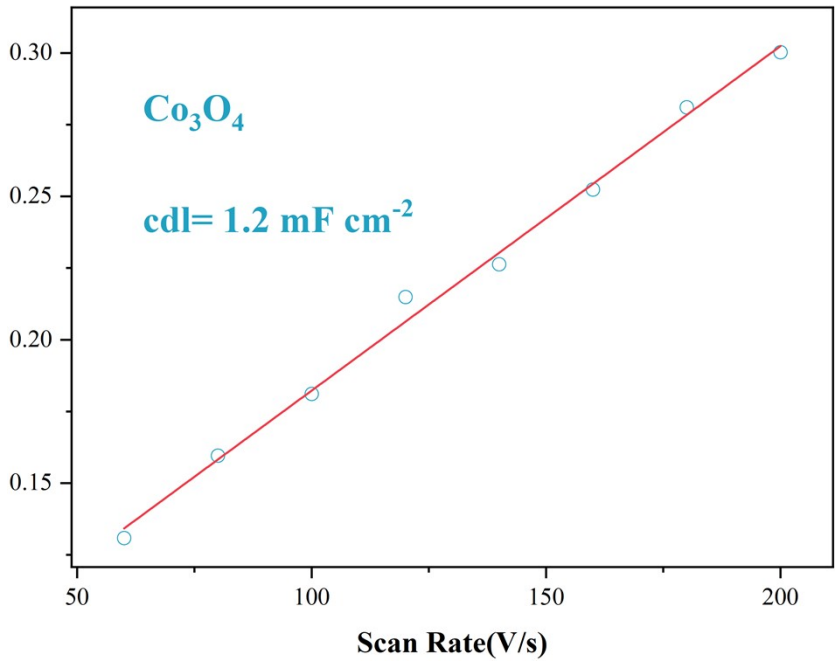

Figure S6. Linear fitting of the capacitive current density differences versus scan rates for Co_3O_4.

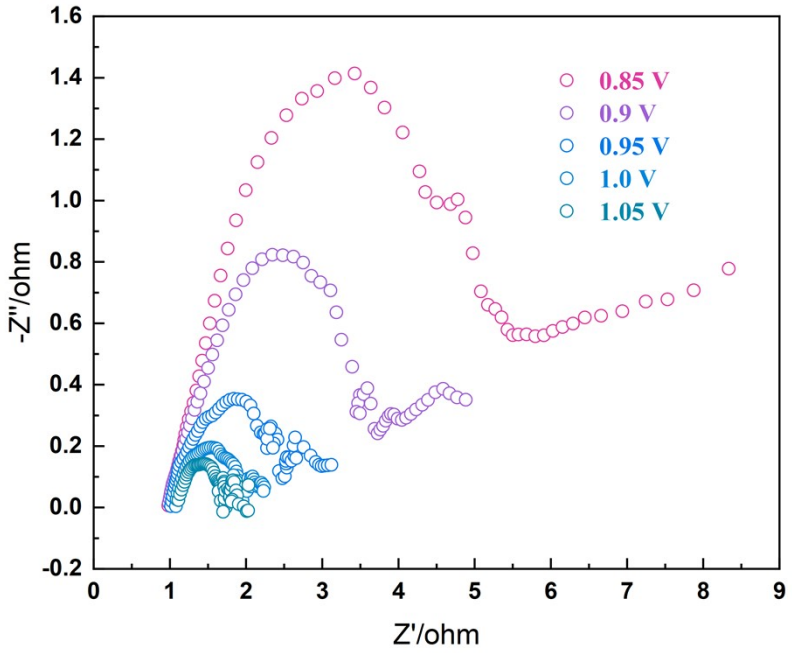

Figure S7. Electrochemical Impedance Spectroscopy (EIS) analysis. Nyquist plots of the RuO_2/Co_3O_4 catalyst recorded at different applied potentials (from 0.85 V to 1.05 V). The reduction in the semi-circle diameter with increasing potential indicates faster charge transfer kinetics at higher driving voltages.

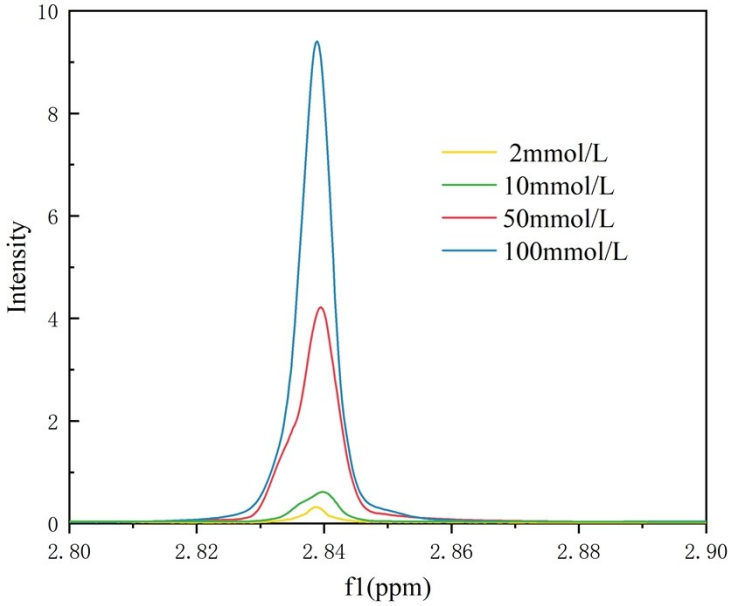

Figure S8. Quantification of Ethylene Oxide (EO). ^{1}H NMR spectra of standard EO solutions with different concentrations (2, 10, 50, and 100 mmol L^{-1}). The characteristic peak of EO is located at approximately 2.84 ppm.

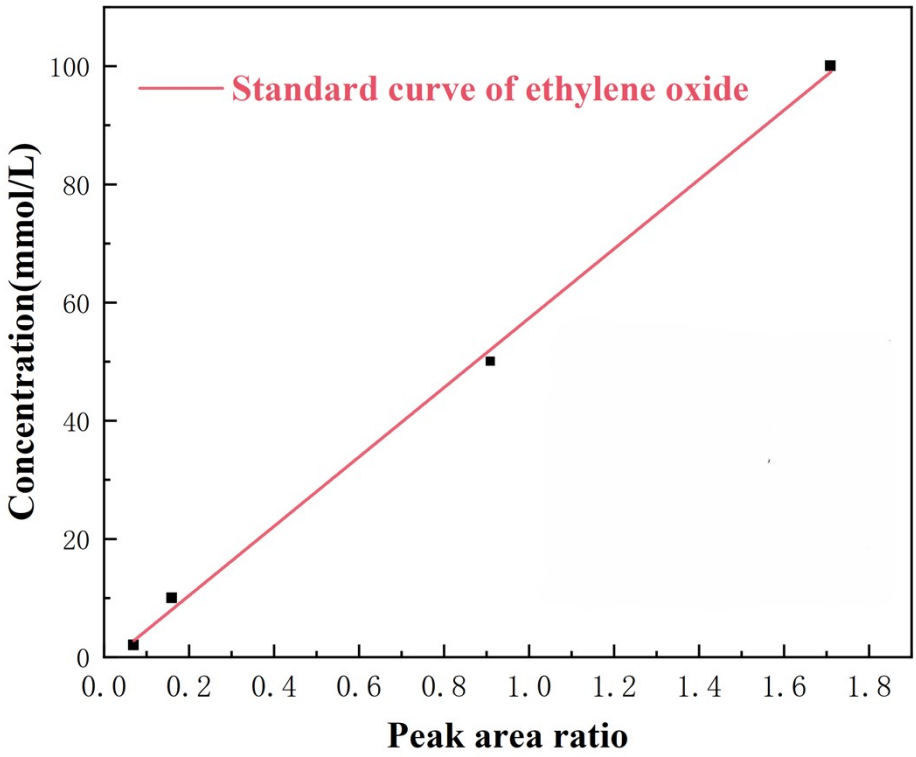

Figure S9. The standard calibration curve derived from the peak areas, showing a good linear relationship ($R^2 > 0.99$) for quantitative analysis.

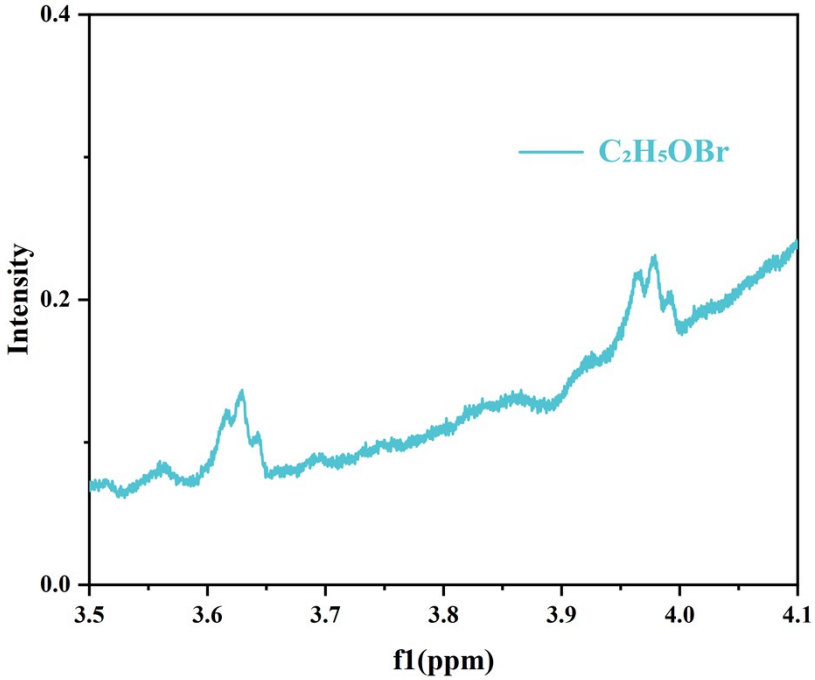

Figure S10. ^{1}H NMR detection of potential liquid by-products. ^{1}H NMR spectrum of 2-bromoethanol (intermediate/byproduct).

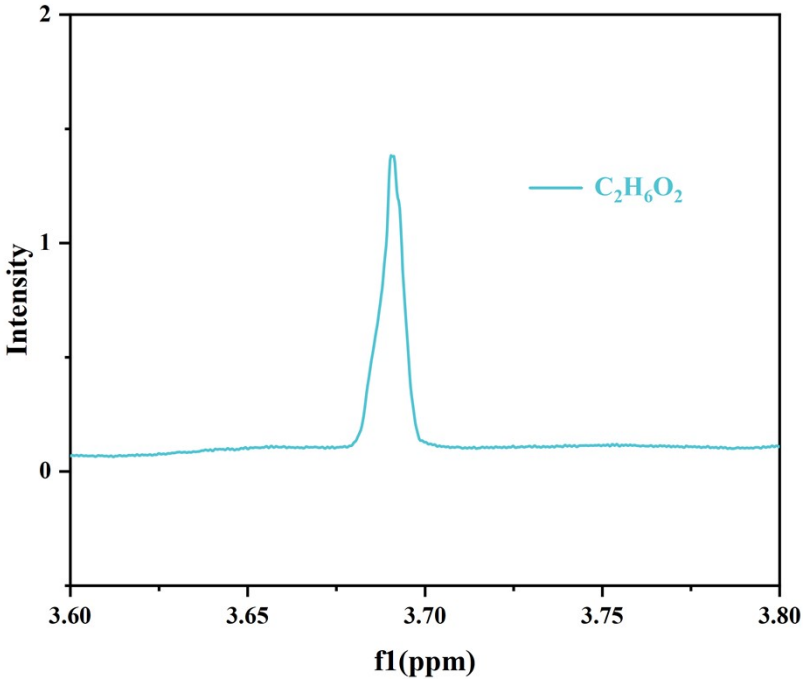

Figure S11. ^{1}H NMR spectrum of ethylene glycol (hydrolysis product). These spectra were used as references to monitor the selectivity of the reaction.

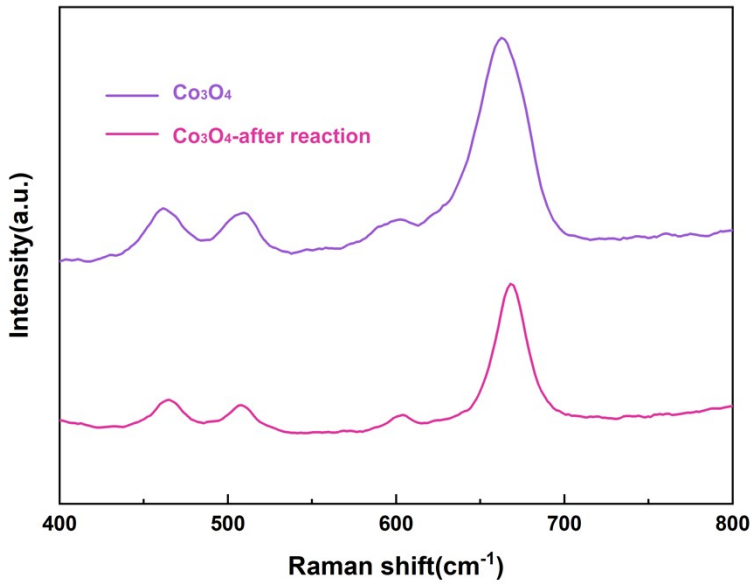

Figure S12. Ex situ Raman spectra of pure Co_3O_4 before and after the BrER stability test. The peak intensity showed obvious decrease after the test.

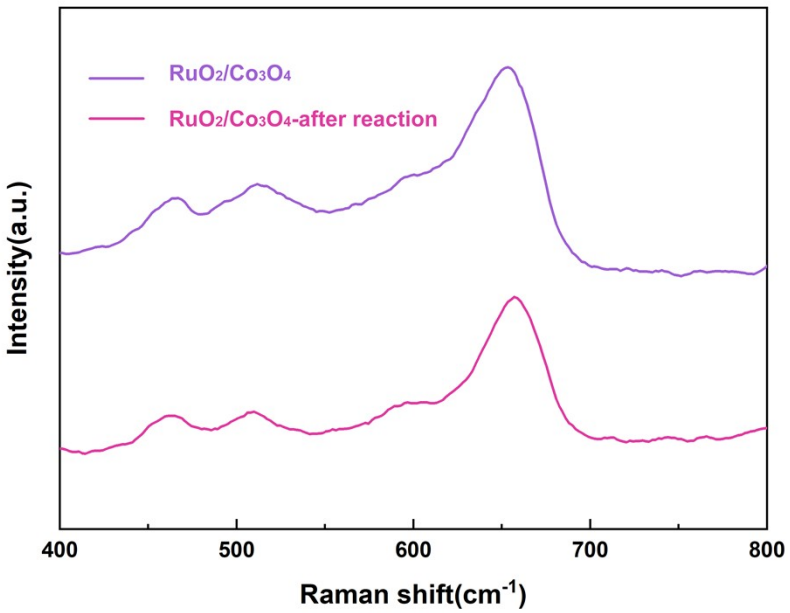

Figure S13. Ex situ Raman spectra of the RuO_2/Co_3O_4 heterojunction before and after the BrER stability test. Almost no change was observed.

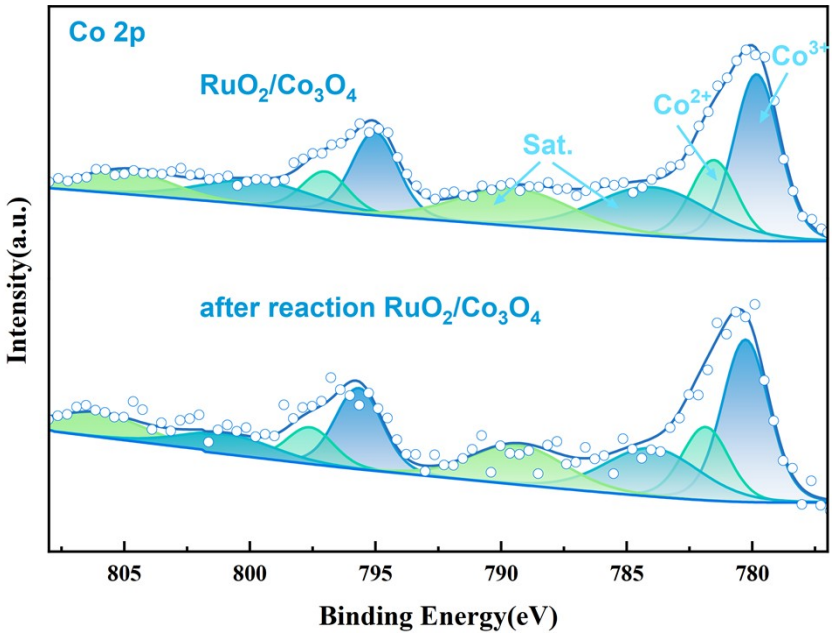

Figure S14. High-resolution Co 2p XPS spectra of the catalysts before and after the long-term BrER stability test for RuO_2/Co_3O_4 heterostructure.

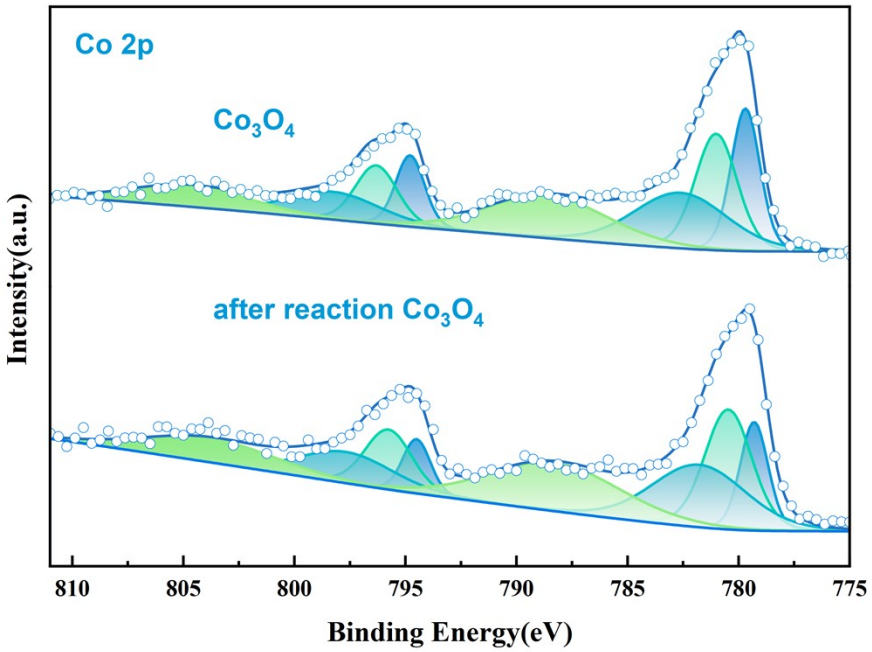

Figure S15. High-resolution Co 2p XPS spectra of the catalysts before and after the long-term BrER stability test for pure Co_3O_4.

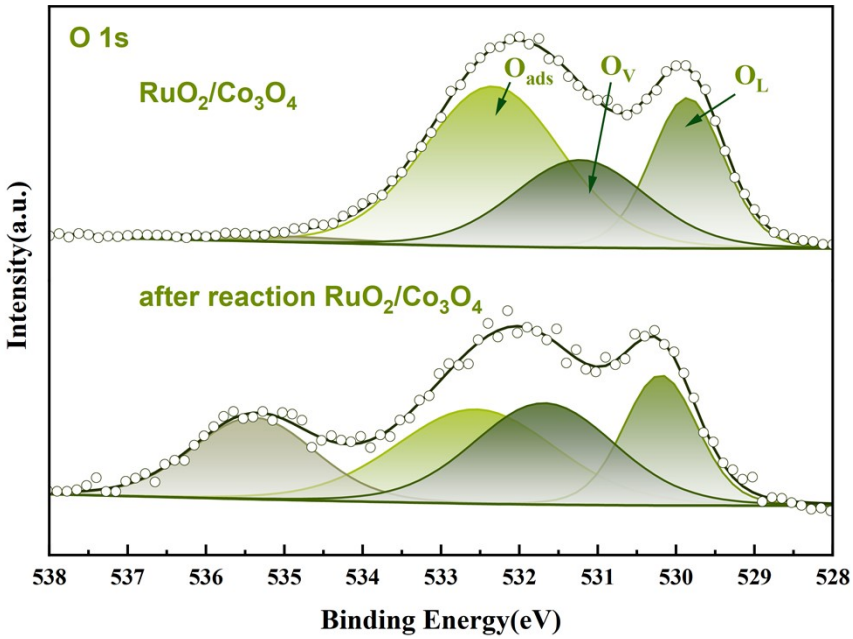

Figure S16. High-resolution O 1s XPS spectra of the catalysts before and after the long-term BrER stability test for RuO_2/Co_3O_4 heterostructure.

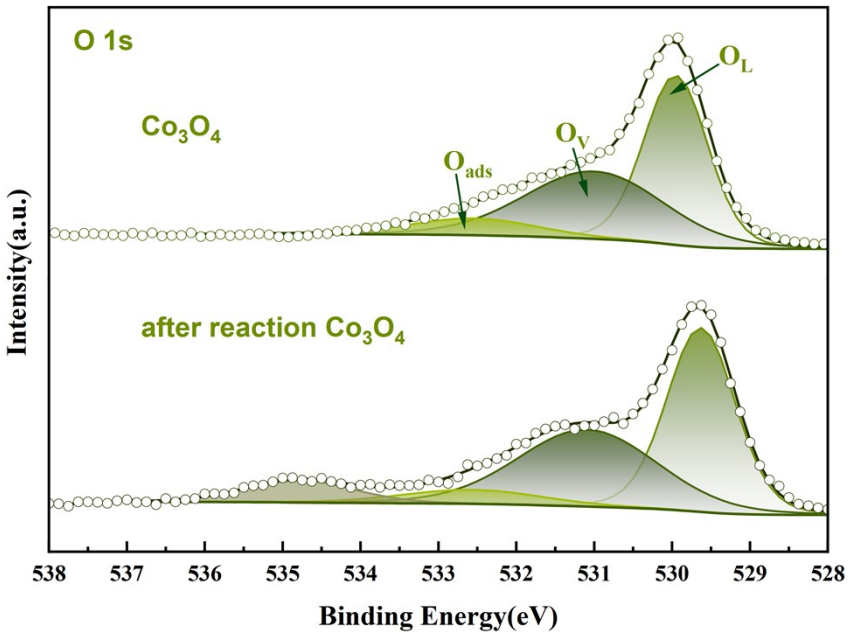

Figure S17. High-resolution O 1s XPS spectra of the catalysts before and after the long-term BrER stability test for pure Co_3O_4.

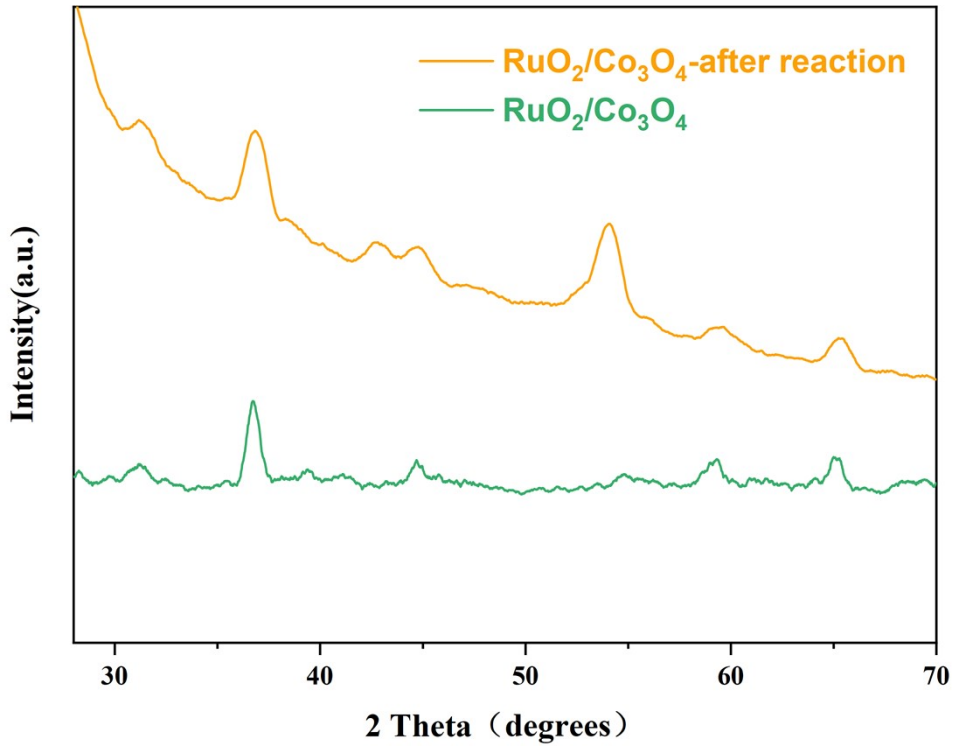

Figure S18. XRD patterns of the RuO_2/Co_3O_4 electrocatalyst before and after the long-term BrER stability test, showing the preservation of the crystal structure.

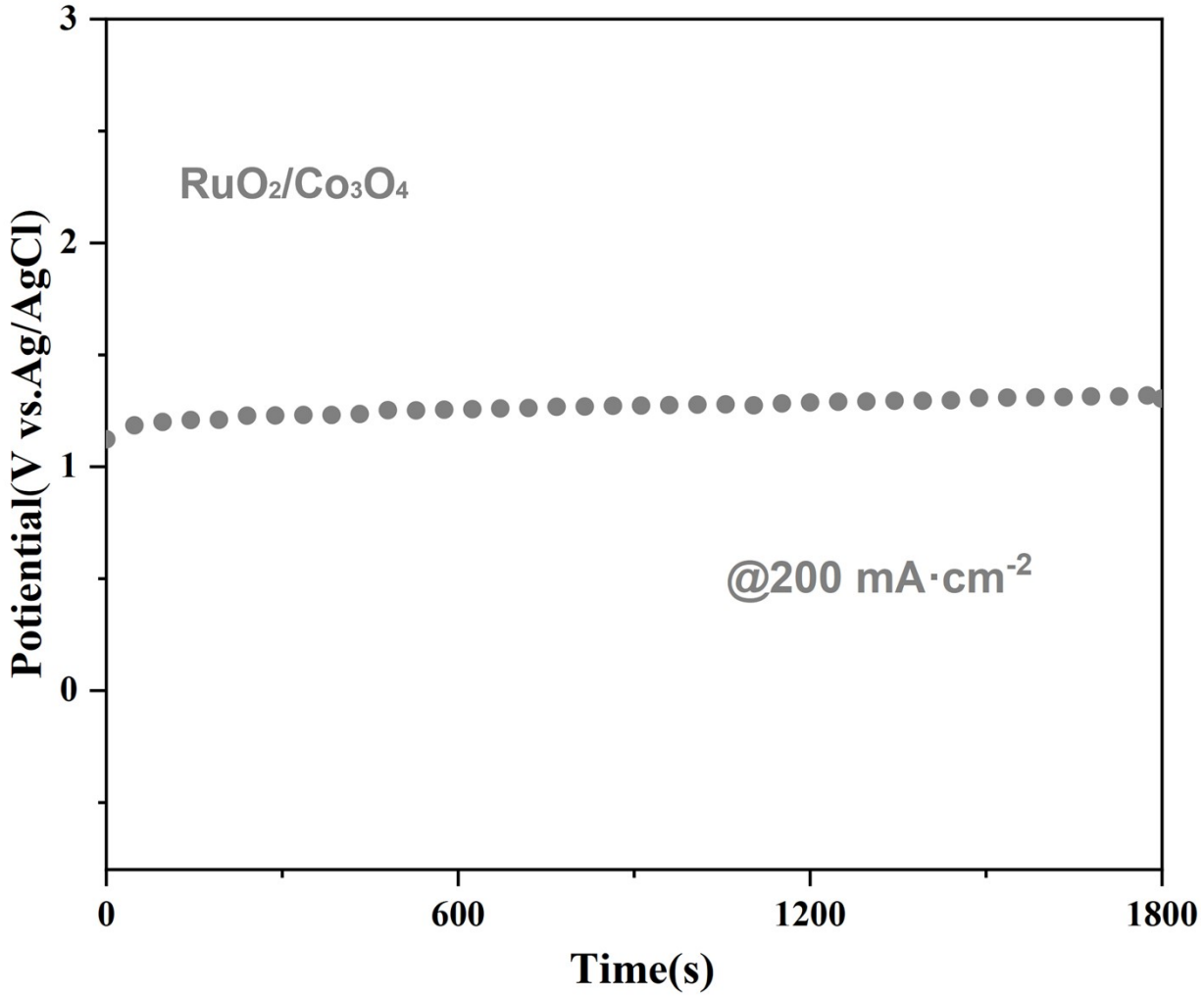

Figure S19. Chronopotentiometry curve of the optimal Ru-10-Co_3O_4 catalyst evaluated at a constant current density of 200 mA cm^{-2}.

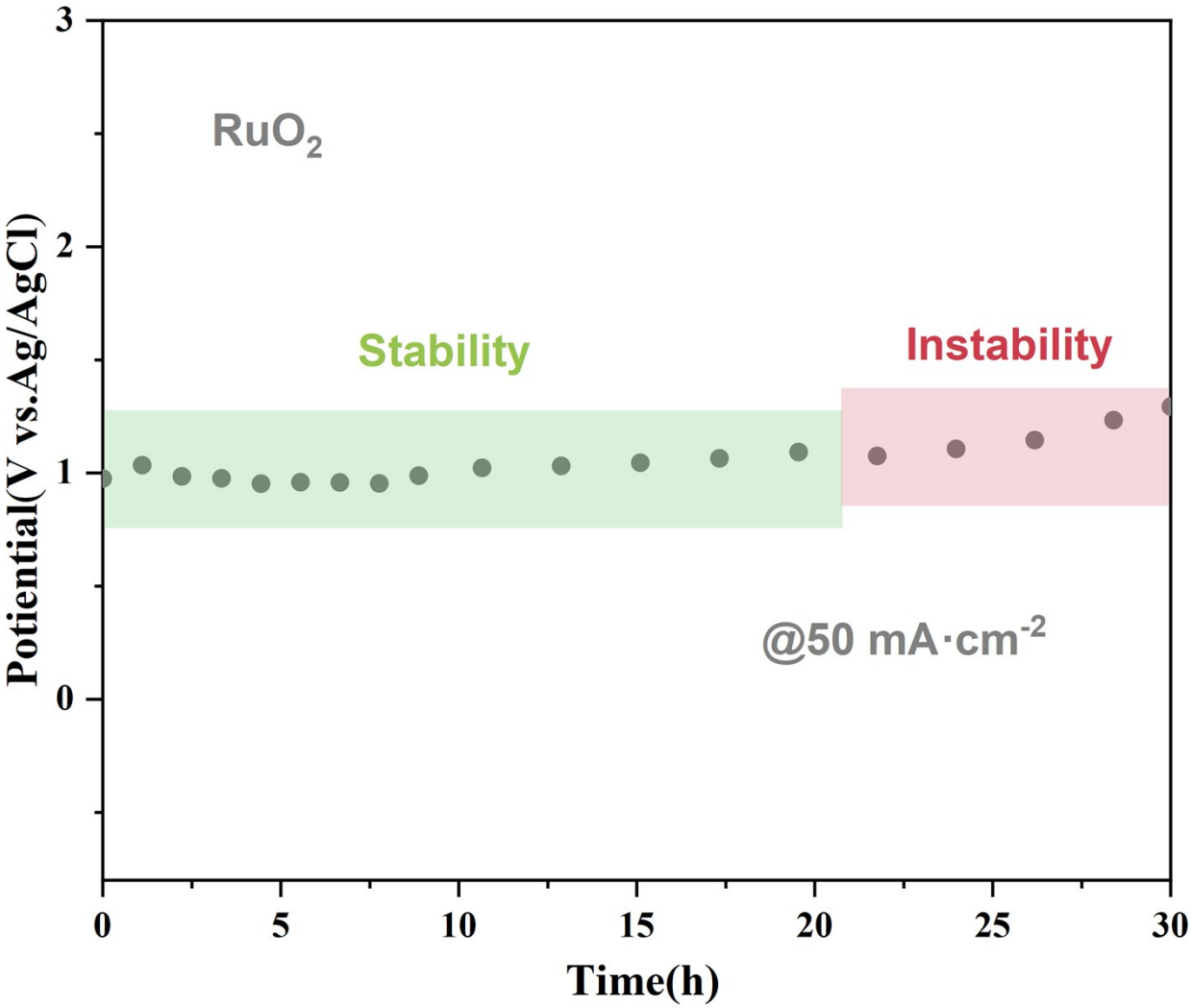

Figure S20. Chronopotentiometry curve of the optimal RuO_2 catalyst evaluated at a constant current density of 50 mA cm^{-2}.

Catalyst	Electrolyte	Current Density (mA cm^{-2})	Voltage / Potential (V)	Faradaic Efficiency	Target Product	Ref.
RuO_2/Co_3O_4	0.5M KBr	200	1.2 V vs. Ag/AgCl	95%	EO	this work
$Ir_{0.1}Ru_{0.9}O_2$	Chloride-rich	150	2.07 V vs. RHE	85.10%	EO	JACS, 2025 (Wang et al.)[11]
$PdPtO_x/C$	Pure water or a mixture of acetonitrile and water	50	1.65 V vs SHE	66 ± 5%	PO	Science, 2024 (Chung et al.)[12]
Pt-RuO_2/TiO_2	0.5 M NaCl or NaBr + 0.1 M $HClO_4$	500	4.7 V (mediated by Cl); 4.3 V (mediated by Br) (cell voltage)	100% (mediated by Cl); >85% (mediated by Br)	EO	Chem. Eng. J., 2024 (Liang et al.)[13]
KIrRuO	1 M KCl	200	2.5 V vs Ag/AgCl	70%	EO	Angew. Chem., 2024 (Wang et al.)[14]
Carbon paper	0.4 M KBr	250	1.9 V vs Ag/AgCl	91%	PO	Nat. Commun., 2024 (Chen et al.)[15]

TS-1/Solid Electrolyte (SE)	DI water	25	2.24 ~ 4.31 V (cell voltage)	63%	EG	Joule, 2023 (Zhang et al.)[16]
BaO_x/IrO_2	2 M KCl	100	3.2 V (cell voltage, without iR compensation)	90%	EO	Nat. Catal., 2022 (Li et al.)[17]
Pt	1.0 ~ 2.0 M KCl	300 - 1000	2.86 V vs. Ag/AgCl	70% ~ 71%	EO	Science, 2020 (Leow et al.)[18]
Co_3O_4 nanoparticles	0.6 M NaCl, pH 8 buffer solution	16.2	1.5 V vs. SHE	47.00%	EO	ACS Catal., 2020 (Chung et al.)[19]
Pt/NCNT	1 M KBr	80.3	1.6 V vs. RHE	92.2%	EO	Angew. Chem., 2023 (Xue et al.)[20]
Ir_1/Co_3O_4	0.5 M NaCl	100	1.85 V vs. RHE	94.8%	EO	Angew. Chem., 2024 (Wang et al.)[14]
IrO_2	0.5 M NaCl	100	1.95 V vs. RHE	87%	EO	Angew. Chem., 2024 (Wang et al.)[14]

Table S1. Summary of key performance metrics (including electrolyte, current density, operating voltage, and Faradaic efficiency) for the electrochemical synthesis of epoxides (EO, PO) and ethylene glycol (EG) over the RuO_2/Co_3O_4 catalyst and other representative advanced electrocatalyst[11-15, 17-24].

References

1. G. Kresse and J. Furthmuller, *Phys Rev B Condens Matter*, 1996, **54**, 11169-11186.
2. M. Ernzerhof and G. E. Scuseria, *The Journal of Chemical Physics*, 1999, **110**, 5029-5036.
3. J. P. Perdew, K. Burke and M. Ernzerhof, *Phys. Rev. Lett.*, 1996, **77**, 3865-3868.
4. G. Kresse and J. Hafner, *Phys Rev B Condens Matter*, 1993, **47**, 558-561.
5. P. E. Blochl, *Phys Rev B Condens Matter*, 1994, **50**, 17953-17979.
6. G. Kresse and D. Joubert, *Phys. Rev. B*, 1999, **59**, 1758-1775.
7. S. Grimme, J. Antony, S. Ehrlich and H. Krieg, *J. Chem. Phys.*, 2010, **132**, 154104.
8. H. J. Monkhorst and J. D. Pack, *Phys. Rev. B*, 1976, **13**, 5188-5192.
9. V. Wang, N. Xu, J.-C. Liu, G. Tang and W.-T. Geng, *Comput. Phys. Commun.* , 2021, **267**.
10. J. K. Norskov, J. Rossmeisl, A. Logadottir, L. Lindqvist, J. R. Kitchin, T. Bligaard and H. Jonsson, *J. Phys. Chem. B* 2004, **108**, 17886-17892.
11. H. Wang, G. Zhang, X. Ma, H. Dong, J. Liu, D. Luo, Z. J. Zhao, T. Wang, P. Zhang and J. Gong, *J. Am. Chem. Soc.* , 2025, **147**, 30222-30229.
12. M. Chung, J. H. Maalouf, J. S. Adams, C. Jiang, Y. Roman-Leshkov and K. Manthiram, *Science*, 2024, **383**, 49-55.
13. N.-N. Liang, W. Choi, D. Suk Han and H. Park, *Chem. Eng. J.* , 2024, **494**.
14. H. Wang, S. Wang, Y. Song, Y. Zhao, Z. Li, Y. Shen, Z. Peng, D. Gao, G. Wang and X. Bao, *Angew. Chem., Int. Ed.*, 2024, **63**, e202402950.
15. M. Chi, J. Ke, Y. Liu, M. Wei, H. Li, J. Zhao, Y. Zhou, Z. Gu, Z. Geng and J. Zeng, *Nat. Commun.*, 2024, **15**, 3646.
16. S.-K. Zhang, Y. Feng, A. Elgazzar, Y. Xia, C. Qiu, Z. Adler, C. Sellers and H. Wang, *Joule*, 2023, **7**, 1887-1901.
17. Y. Li, A. Ozden, W. R. Leow, P. Ou, J. E. Huang, Y. Wang, K. Bertens, Y. Xu, Y. Liu, C. Roy, H. Jiang, D. Sinton, C. Li and E. H. Sargent, *Nat. Catal.*, 2022, **5**, 185-192.
18. W. R. Leow, Y. Lum, A. Ozden, Y. Wang, D. H. Nam, B. Chen, J. Wicks, T. T. Zhuang, F. Li, D. Sinton and E. H. Sargent, *Science*, 2020, **368**, 1228-1233.
19. M. Chung, K. Jin, J. S. Zeng and K. Manthiram, *ACS Catal.*, 2020, **10**, 14015-14023.
20. W. Xue, L. Quan, H. Liu, B. Yu, X. Chen, B. Y. Xia and B. You, *Angew. Chem., Int. Ed.*, 2023, **62**, e202311570.
21. R. Xia, Y. Chen, Y. Chang, H. Shin, H. Ze, H. Liu, P. Ou, R. Dorakhan, S. Park, P. Papangelakis, Z. Guo, E. G. Machado, M. V. Reboucas, M. Nikkhoo, R. G. A. Duarte, D. Zhou, Y. Liu, W. Ni, C. Tian, Y. Chen, C. Yu, O. K. Farha, K. Xie and E. H. Sargent, *Nat. Catal.*, 2025, **8**, 833-842.
22. A. Z. Li, B. J. Yuan, M. Xu, Y. Wang, C. Zhang, X. Wang, X. Wang, J. Li, L. Zheng, B. J. Li and H. Duan, *J. Am. Chem. Soc.* , 2024, **146**, 5622-5633.
23. S. Iguchi, M. Kataoka, R. Hoshino and I. Yamanaka, *Catal. Sci. Technol.*, 2022, **12**, 469-473.
24. L. Cai, Y. Liu, Y. Gao, B. H. Zhao, J. Guan, X. Liu, B. Zhang and Y. Huang, *Angew. Chem., Int. Ed.*, 2025, **64**, e202417092.